

CeO₂ Nanoparticle Morphologies and Their Corresponding Crystalline Planes for the Photocatalytic Degradation of Organic Pollutants

Rafael A. C. Amoresi,^{*,†} Regiane C. Oliveira,^{†,‡} Naiara L. Marana,[‡] Priscila B. de Almeida,[§] Paloma S. Prata,^{||} Maria A. Zaghete,[⊥] Elson Longo,[§] Julio R. Sambrano,[‡] and Alexandre Z. Simões[†]

[†]Faculty of Engineering of Guaratinguetá, São Paulo State University, UNESP, 12516-410 Guaratinguetá, SP, Brazil

[‡]Modeling and Molecular Simulations Group, São Paulo State University, UNESP, 17033-360 Bauru, SP, Brazil

[§]Interdisciplinary Laboratory of Electrochemistry and Ceramics, LIEC, Department of Chemistry, Universidade Federal de São Carlos, UFSCAR, 13565-905 São Carlos, SP, Brazil

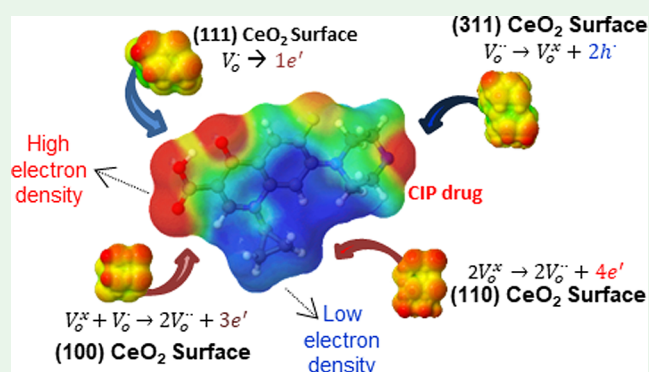
^{||}UFSCar, Department of Chemistry, Universidade Federal de São Carlos, UFSCAR, 13565-905 São Carlos, SP, Brazil

[⊥]Interdisciplinary Laboratory of Electrochemistry and Ceramics, LIEC, Chemistry Institute, São Paulo State University, UNESP, 14800-060 Araraquara, SP, Brazil

Supporting Information

ABSTRACT: Currently, numerous properties of semiconducting oxides are correlated to their morphological characteristics resulting from their exposed surfaces. In the present work, the relationship between the following morphologies rod, bean, hexagon, and rod/cube of CeO₂ with the exposure of (111), (110), (100), and (311) surfaces and the main charge carriers generated by the photochemical processes was investigated. This was done in regard to the degradation of ciprofloxacin and rhodamine-B. The initial stages of the degradation of the two types of molecules were evaluated, allowing the determination of where the charge carriers generated in the semiconductor preferentially acted on the molecules. Therefore, the active species in each photocatalyst were identified by scavenger tests and correlated to the computational simulations using the density functional theory. Accordingly, the relationships between the morphology, surface exposure in the particles, surface defects, photochemically generated species, and preferential attack on the micropollutant molecule were shown. Specific surface area analyses demonstrate an effective relationship between photocatalytic activity and the exposed surface of the particle. This will allow rationalization of the relation between the catalytic and electronic properties of semiconductor surfaces.

KEYWORDS: CeO₂, surface, scavengers, CIP, DFT



1. INTRODUCTION

Several studies have focused on the relationship between the preferential growth of semiconductors in a given direction, i.e., on morphological control, and their properties.^{1–3} Relations such as the following were found to exist: preference of catalytic conversion of CO on the {100} and {101} surfaces of Au/TiO₂ materials;⁴ improvement in the magnetic properties when (001) and (111) surfaces are exposed to MnTiO₃ due to the surface composition of the [TiO_n] reduced species;⁵ and increase in the photocatalytic properties of the exposed (011) and (010) surfaces in ZnWO₄ monoclinic materials due to the presence of holes (h⁺).⁶ The relationship between the material morphology and resulting properties was also verified for cerium oxide, CeO₂, by Mai et al.⁷ It was observed that the surface structures dominated by {100}/{110} facets with rod-

like morphologies were more reactive to CO oxidation and exhibited a higher capacity to store oxygen on the surface compared to surface materials dominated by {111} facets with a polyhedron morphology.

CeO₂ is an n-type semiconductor of cubic crystalline structure with a band gap of about 3.2 eV, and it exhibits different properties depending on its morphology.⁸ This semiconductor has a high oxygen storage capacity and oxygen vacancy mobility as observed by the easy conversion between its oxidation states, Ce⁴⁺ and Ce³⁺.⁹ Ma et al.¹⁰ synthesized CeO₂/gC₃N₄ compounds and evaluated the photocatalytic

Received: July 31, 2019

Accepted: September 17, 2019

Published: September 17, 2019



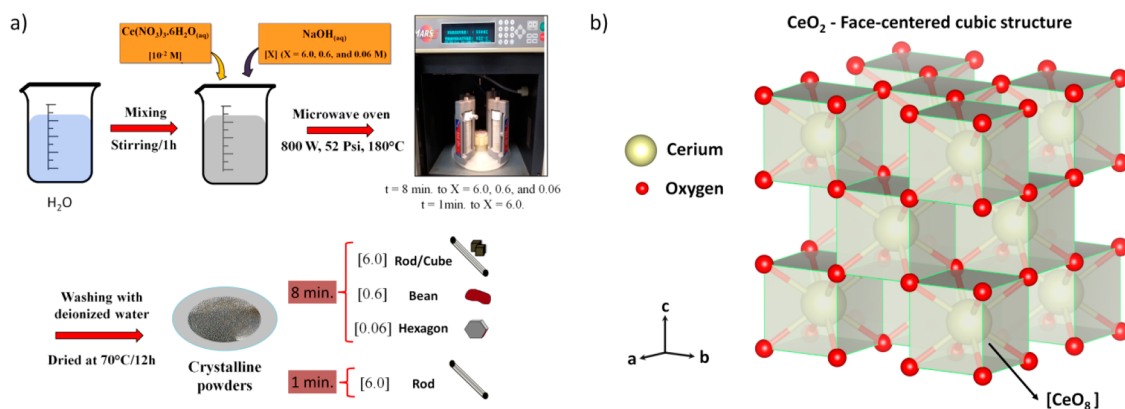


Figure 1. (a) Illustrated scheme of the microwave-assisted hydrothermal method used for the nanoparticles synthesis and (b) chemical structure of the unit cell of CeO_2 .

activity of pure and composite materials. They found that the composite has higher photocatalytic performance due to the better separation and migration of photogenerated charge carriers. Feng et al.¹¹ evaluated several CeO_2 morphologies for the catalytic combustion of toluene for CO_2 and water mineralization. They observed that hollow-sphere morphologies presented better activity because their surface was composed mainly of (111) planes, resulting in more oxygen vacancies. Recently, Ma et al.¹² published a review revealing the fundamental mechanisms of photocatalytic performance in relation to modifications in CeO_2 by metal doping, nonmetal doping, deposition of noble metals on the surface, hetero-junctions, and the most important factors that influence and promote the separation and recombination of e^-/h^+ pairs to photocatalytic activity. It is known that the catalytic or photocatalytic performance as high reaction rate, photochemical activation spectroscopic range, and stability of semiconductor materials are dependent on the composition,^{13,14} exposed surface,^{5,11} and the oxidative or reducing agents generated in them.¹⁵ Regarding catalytic activity, both the adsorption site of the molecule with its predominant functional groups and the agents generated in the semiconductor (by photocatalysis) are related to the catalytic/photocatalytic efficiency.^{16–18}

Commonly, dye molecules are used to evaluate the photocatalytic efficiency of a semiconductor material.^{15,19,20} These are chromophoric molecules with absorption in the visible region. Generally, they are initially degraded by the de-ethylation of their outermost organic groups, followed by the degradation of the aromatic rings²¹ by agents such as the h^+ generated by the semiconductor.^{6,15} Other types of molecules, e.g., drugs, can possess multiple functional groups and may present an amphoteric behavior,²² which suggests that a photocatalyst may have different possible degradation mechanisms. The above-mentioned groups include ciprofloxacin, CIP ($\text{C}_{17}\text{H}_{18}\text{FN}_3\text{O}_3$), an antibiotic of second-generation fluoroquinolone, which consists of a quinolone structure and piperazine moiety.^{23,24} This drug is widely administered as both a human and veterinary medicine and currently holds the fourth position in the European antibiotic market.^{25–27} It is the most frequently detected antibiotic in wastewater treatment plants and raw drinking water²⁸ because most wastewater treatment plants cannot eliminate it effectively. Therefore, seeking an efficient strategy to eliminate CIP from wastewater is still imperative.

According to several works related to photocatalytic activity, in semiconductors with a spherical-type morphology²⁹ with surfaces exposed in different directions, it is difficult to verify which surface has the dominant influence on the degradation mechanism. CeO_2 with different morphologies was previously studied and found to exhibit different photocatalytic activities according to its morphology.³⁰ However, analyses considering the type of exposed surface for each morphology and the mechanism responsible for the photocatalysis were not verified.

Here, we report the synthesis of CeO_2 nanoparticles by a microwave-assisted hydrothermal (MAH) method. We investigated the relationship of different CeO_2 morphologies with the respective exposed crystalline planes, generated agents ($\cdot\text{O}_2$, $\cdot\text{OH}$, h^+), and interaction with the pollutant undergoing degradation. The structural, electronic, optical, and degradation properties were correlated to the morphology. Field-emission scanning electron microscopy (FE-SEM), high-resolution transmission electron microscopy (TEM), X-ray diffraction (XRD), micro-Raman scattering spectroscopy, ultraviolet–visible (UV–vis) spectroscopy, and mass spectroscopy were employed to characterize the samples. Computational simulations were performed with periodic density functional theory (DFT) to study the theoretical band gap, surface energy, Mulliken charges, and alignment between the bands of each surface. The experimental and theoretical results are reported for the understanding of the relation between the structural and electronic parameters of each CeO_2 nanoparticle surface with the main radicals generated by the photocatalytic activity during the degradation of the molecules.

2. EXPERIMENTAL SECTION

2.1. Synthesis. CeO_2 nanoparticles were obtained by an MAH method (Figure 1a). The procedure for the preparation consisted of dissolving cerium nitrate hexahydrate ($\text{Ce}(\text{NO}_3)_3 \cdot 6\text{H}_2\text{O}$, 99%, neon), $0.06 \text{ mol} \cdot \text{L}^{-1}$, in 90 mL of NaOH, $X \text{ mol} \cdot \text{L}^{-1}$ (where $X = 6.0, 0.6$, and $0.06 \text{ mol} \cdot \text{L}^{-1}$), and the mixture was stirred for 1 h at 25°C . The suspension was placed in a microwave oven at $180^\circ\text{C}/8 \text{ min}$. The powders were washed with deionized water several times and dried at $70^\circ\text{C}/12 \text{ h}$. For each synthesis, the concentration of NaOH was varied, with $X = 6.0, 0.6$, and $0.06 \text{ mol} \cdot \text{L}^{-1}$ resulting in morphologies of the type rod/cube, bean, and hexagon, respectively. The synthesis with NaOH $6.0 \text{ mol} \cdot \text{L}^{-1}$ and a microwave time of 1 min (at $180^\circ\text{C}/1 \text{ min}$) resulted in a rod-type morphology.

2.2. Characterization. The CeO_2 nanocrystals were structurally characterized via XRD patterns using a D/Max-2000PC diffractometer, Rigaku (Japan), with $\text{Cu K}\alpha$ radiation ($\lambda = 1.5406 \text{ \AA}$) in the 2θ range from 20° to 90° . The Raman spectroscopy characterization was

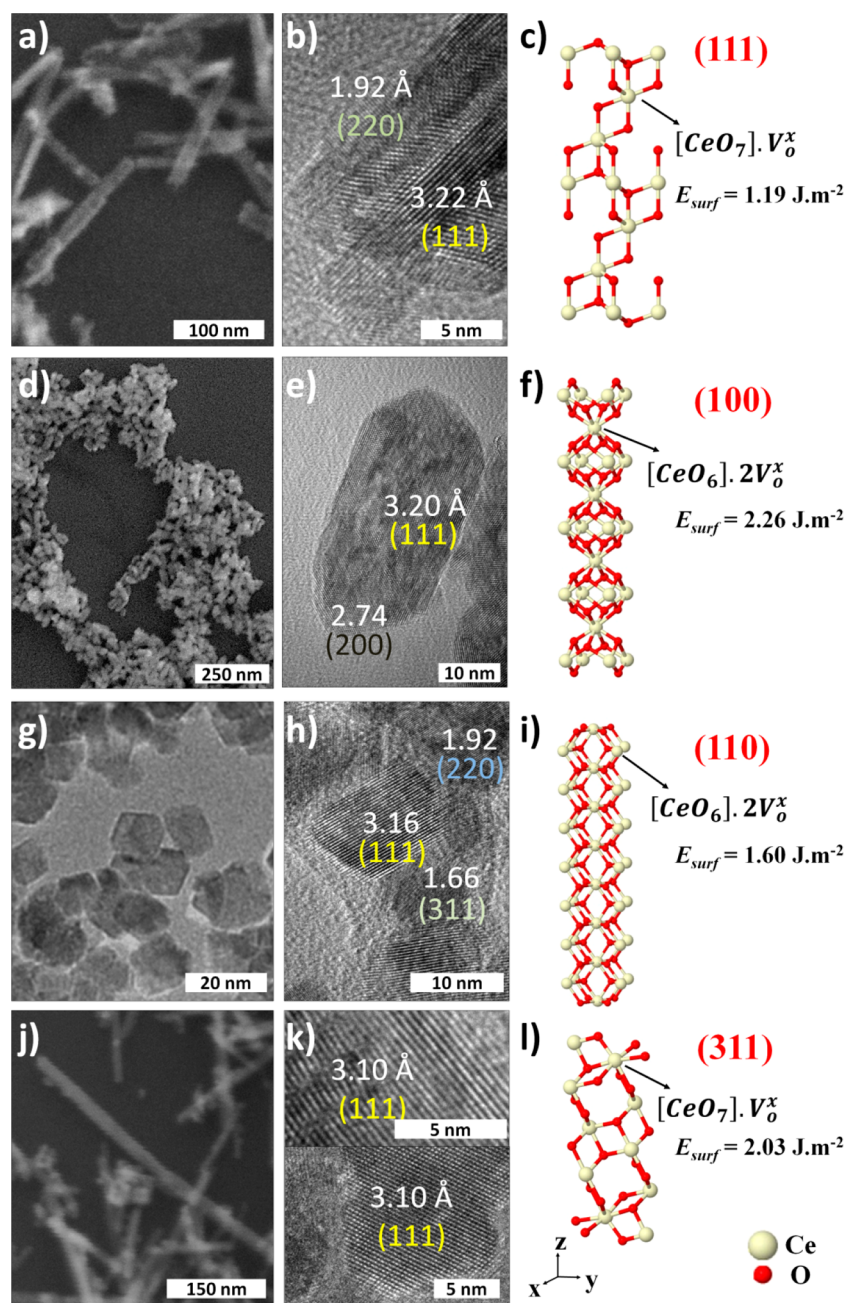


Figure 2. FE-SEM and HRTEM images of the different morphologies obtained for CeO₂: (a, b) rod, (d, e) bean, (g, h) hexagon, and (j, k) rod/cube type. The HRTEM images show *d*-spacings for each region in the particle: (a) the rod-type sample has exposed (111) and (220) planes; (b) the bean-type sample has exposed (111) and (200) planes; (c) the hexagon-type sample has exposed (111), (220), and (311) planes; (d) the rod/cube-type sample has exposed (111) and (200) planes. The surface models for each morphology of the CeO₂ nanocrystals are shown for (c) (111), (f) (100), (i) (110), and (l) (311) surfaces.

performed by a LabRAMiHR550 Horiba JobinYvon spectrometer with a laser of 514 nm as the excitation source and a spectral resolution of 1 cm⁻¹, with 40 scans in the range of 50–1000 cm⁻¹. The particle morphology was investigated via HR-TEM, TEM-FEI/PHILIPS CM120 microscopy, and a field-emission scanning electron microscope, model FE-SEM Inspect F50 (FEI Company, Hillsboro, OR), operated at 5 kV. X-ray photoelectron spectroscopy (XPS) measurements were performed using a Scienta Omicron ESCA+ spectrometer system equipped with a hemispherical analyzer (EA125) and a monochromatic source of Al K α ($h\nu = 1486.7$ eV). The spectra were corrected to the charge effects using the C 1s peak of adventitious carbon at 284.6 eV as a reference. All data analyses were made using CASA XPS software (Casa Software Ltd., U.K.). The photonic characteristics were analyzed by UV–vis diffuse reflectance

using a PerkinElmer UV/vis/NIR Lambda 1050 spectrophotometer. BET specific area was carried out using ASAP 2010 Micromeritics equipment. Photocatalytic experiments were performed using 15 mg of the photocatalyst (0.3 g L⁻¹) which was added to 50 mL of the CIP drug solution (10⁻⁵ mol L⁻¹) (or of pattern rhodamine-B (Rh-B) dye 10⁻⁵ mol L⁻¹ solution). Before irradiation, the suspension was magnetically stirred for 45 min in the dark at room temperature to achieve the adsorption/desorption equilibrium. After that, the suspension was illuminated by six lamps (lamp $\lambda_{\max} = 254$ nm, PHILIPS TL-D, 15 W) (~ 9.55 mW/cm² at the center of the reaction vessel) with air bubbling and constant stirring. In situ capture photocatalytic experiments using scavengers were conducted to capture the active species in the semiconductor and predict the degradation mechanism. The compounds used as scavengers were

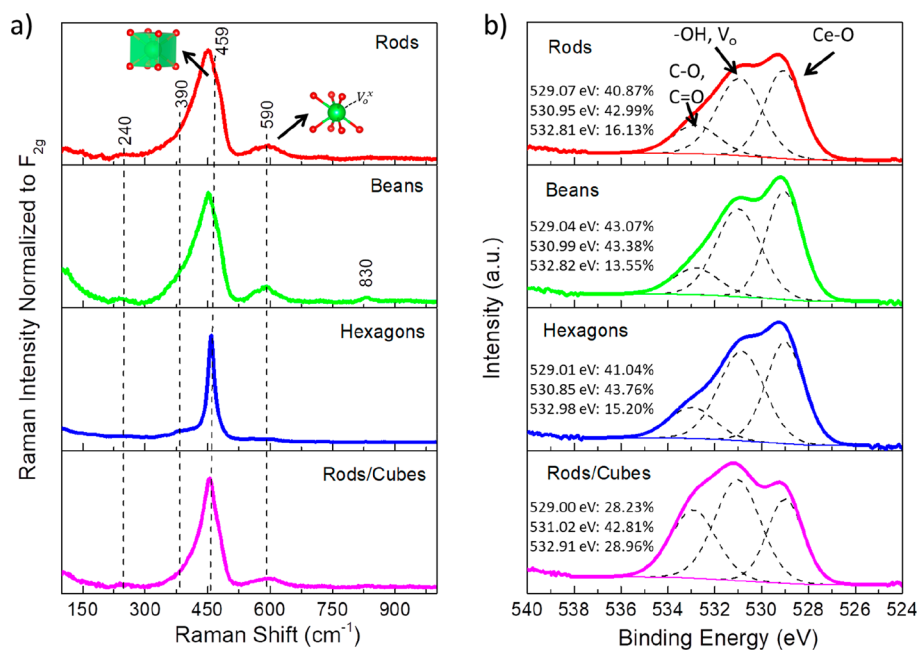


Figure 3. (a) Experimental room-temperature Raman spectra (514.5 nm) in the range from 50 to 1000 cm⁻¹ and (b) high-resolution XPS for the O 1s species for different morphologies of the CeO₂ powder samples.

ammonium oxalate (88 mg), *p*-benzoquinone (67 mg), and isopropanol (0.048 mL). Aliquots were withdrawn at certain times, centrifuged, and analyzed via absorption spectroscopy using a spectrophotometer (Femto Cirrus 80PR). Electrospray ionization mass spectrometry (ESI-MS) analysis was performed by positive ESI using a Waters XevoG2-XS QT of quadrupole/time-of-flight mass spectrometer by direct infusion with a flow rate between 1 and 10 μL/min. The mass spectra were recorded from *m/z* 100 to *m/z* 2000 for the purpose of identification.

3. COMPUTATIONAL SIMULATION

DFT simulations were conducted using the CRYSTAL17 program³¹ with the WC1LYP (8% hybrid) functional.³² The oxygen atoms were described by all-electron basis set, O_6-31d1,³³ whereas the cerium atoms were described by the effective core pseudopotential (ECP) basis set, Ce_ECP.³⁴ The integration process was performed using the option XXLGRID (extra-extra-large grid), containing 99 radial and 1454 angular points. The accuracy of the truncation criterion for the bioelectronic integrals (Coulomb and Hartree–Fock (HF) exchange series) was controlled by a set of five thresholds (10⁻⁸, 10⁻⁸, 10⁻⁸, 10⁻⁸, and 10⁻¹⁶). These parameters represent respectively the overlap and penetration of the Coulomb integrals, overlap of the HF exchange integrals, and pseudo-overlap in the HF exchange series. In the self-consistent field (SCF) procedure, the shrinking factor for both the diagonalization of the Fock matrix and calculation of the energy was set as 6, corresponding to 16 independent *k*-points in the irreducible part of the Brillouin zone.

The equilibrium structure of CeO₂ is face-centered cubic (fcc) structure, with space group *Fm* $\bar{3}$ *m*, which in the bulk has cerium ions octahedrally coordinated with oxygen ions, forming clusters of the type [CeO₈], Figure 1b. Each exposed surface exhibits variation in the anion and cation coordination. As a first procedure, bulk optimization of the CeO₂ structure was performed to determine the equilibrium geometry. As a second step, the (100), (110), (111), and (311) surfaces were unreconstructed (truncated bulk) slab models using the

calculated equilibrium geometry while considering the mirror symmetry with respect to the central layers. These slabs were finite in the *z*-direction but periodic in the *x*- and *y*-directions. Full relaxation of these surfaces was performed. The surface stability and crystal morphologies were discussed in terms of the surface energy (E_{surf}) obtained by $E_{\text{surf}} = E_{\text{slab}} - nE_{\text{bulk}} / (2A)$, where E_{slab} and E_{bulk} correspond to the optimized surfaces and bulk, respectively, *n* is the number of CeO₂ units on each surface, and *A* is the surface area.

4. RESULTS AND DISCUSSION

4.1. Structure and Morphology. For all the obtained samples, the structural properties at long-range order, as presented in Figure S1, showed a cubic structure with space group *Fm* $\bar{3}$ *m* (ICSD pattern no. 239412) for CeO₂. The obtained theoretical parameter, $a = 5.39$ Å, is in good agreement with the experimental values. No additional reflections were found in the XRD patterns, suggesting a high purity. Parts a, d, g, and j of Figure 2 show the FE-SEM images, and different morphologies are observed for all the samples. The different morphologies obtained are related to the mineralizer agent concentration employed for the particle growth.^{7,35} Since surface free energy is directly associated with surface energy and surface area,³⁶ the change in concentration of adsorbent ions alters the isotropic particle growth. Increasing the concentration of the NaOH as the mineralizing agent (i.e., the increase in OH⁻ during synthesis) associated with precipitation and nucleation sequences^{37,38} favors the nanostructure anisotropy. The particle shape changes from a more symmetrical morphology (hexagon) to less symmetrical morphologies (bean and then rod). In Figure 2a, it is possible to observe the predominance of nanoparticles with rod-type morphologies. Figure 2d shows a bean-type morphology. Figure 2g illustrates the morphological characteristics of a hexagon type, whereas in Figure 2j, there is a mix of rod- and cube-type morphologies for nanoparticles.

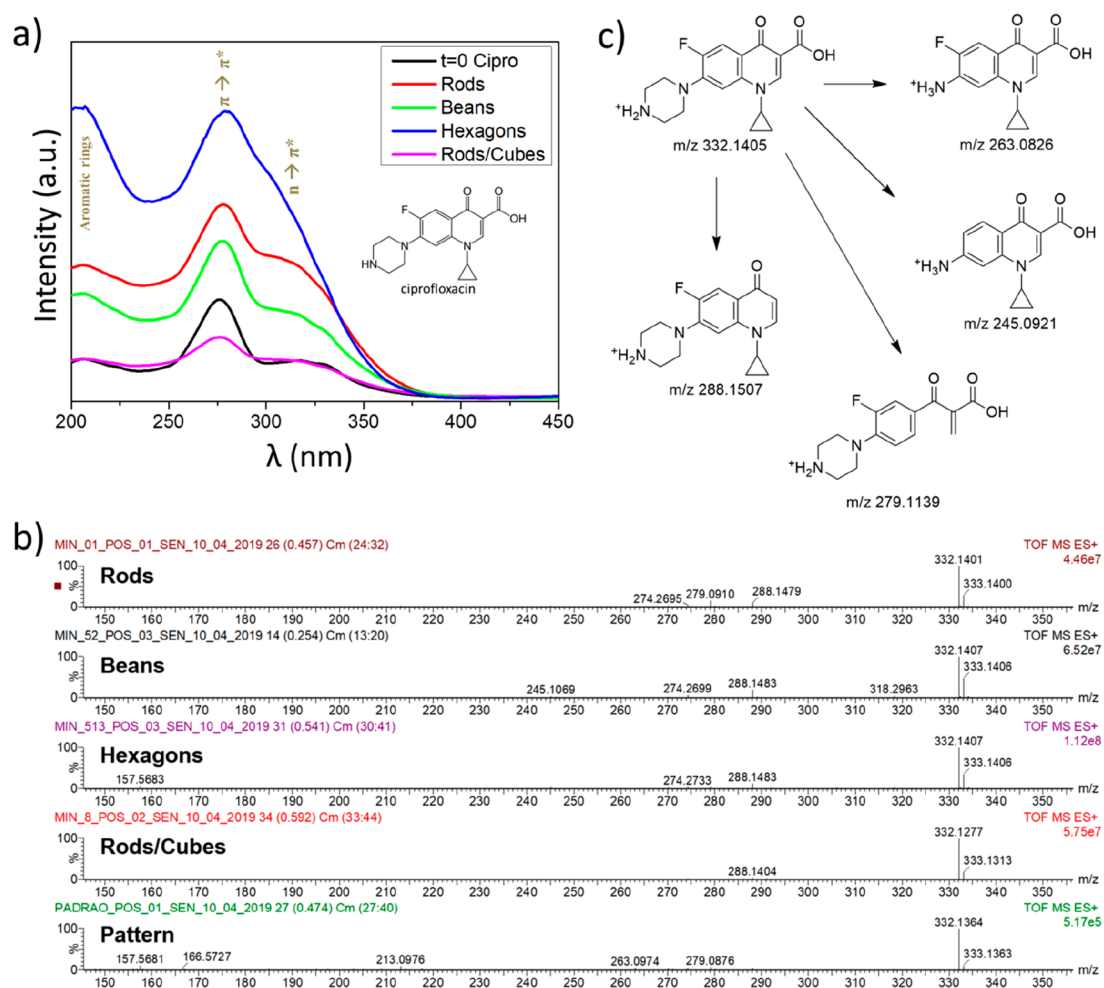


Figure 4. Photocatalytic activity for the degradation of ciprofloxacin drug: (a) absorption spectra for the drug before the start of the photocatalysis, showing the molecule and main transitions in the spectra, and the photocatalytic activity after 60 min of the degradation with different morphologies of CeO₂; (b) ESI(+)-MS spectra of the CIP intermediates that appeared in the photochemical process; (c) proposed scheme for the fragmentation of the CIP intermediates.

HRTEM analyses were performed to elucidate the crystalline planes of the CeO₂ nanoparticle surface for the different morphologies obtained, which are shown in parts b, e, h, and k of Figure 2. Figure 2b shows rod-CeO₂ with distances of 3.22 and 1.92 Å corresponding to the *d*-spacings of (111) and (220) planes, respectively. Figure 2e exhibits bean-CeO₂ nanoparticles with calculated distances of 3.20 and 2.74 Å to the crystalline planes. These are in good agreement with the *d*-spacings of (111) and (200) planes, respectively. Figure 2h shows hexagon-shaped particles, with distances 3.16 Å, 1.92 Å, and 1.66 Å corresponding to the *d*-spacings of (111), (220), and (311) planes, respectively. A mixture of nanoparticles with rod and cube-type shapes is shown in Figure 2k. For both the nanoparticles, only a 3.10 Å distance corresponding to the *d*-spacing of (111) plane is observed. In agreement with the XRD results, all the calculated distances and their respective crystalline planes correspond to the cubic CeO₂ phase.

Parts c, f, i, and l of Figure 2 depict the simulated CeO₂ surfaces and the calculated stability order of the surfaces using the equation of surface energy (E_{surf}). The figure shows different types of [CeO_{*x*}]^{*x*} clusters of these surfaces in the presence of oxygen vacancies, V_O^{*x*}. According to the surface energy, the order of surface stability is (111) < (110) = (220) < (311) < (100) = (200). Specifically, the (111) surface is the

most stable surface with $E_{\text{surf}} = 1.19 \text{ J}\cdot\text{m}^{-2}$, whereas the (100) and (200) surfaces are the less stable with $E_{\text{surf}} = 2.26 \text{ J}\cdot\text{m}^{-2}$. The stability of the (111) plane can explain the reason it appears in all the obtained morphologies and also the photocatalytic activity trend, which will be discussed below.

The Raman scattering spectra for the different CeO₂ morphologies elucidate structural distortions in the short-range order, as shown in Figure 3a. The spectra of the rod, bean, hexagon, and rod/cube morphologies are shown. In these spectra the predominant bands are at 390, 459, and 590 cm⁻¹. These bands correspond to a second-order transverse acoustic (TA) scattering mode, tridegenerate mode (F_{2g}) attributed to the symmetrical stretching vibrations of the O²⁻ ions neighboring the Ce⁴⁺ ion, and mode induced by a defect (D) related to the presence of oxygen vacancies,¹¹ respectively. By comparing the Raman spectra obtained for the samples with rod or bean morphology with the spectrum obtained for the samples with hexagon or rod/cube morphologies, we can see that the F_{2g} mode shifts to a lower energy from 459 to 450 cm⁻¹, and there is an appearance of a band at 240 cm⁻¹ related to a TA mode. For the bean-type morphology, a mode appears at a high energy corresponding to 830 cm⁻¹ related to a transverse optic, TO, mode.^{39,40} The spectra of the hexagon and rods/cubes samples exhibit modes at 390 and 459 cm⁻¹,

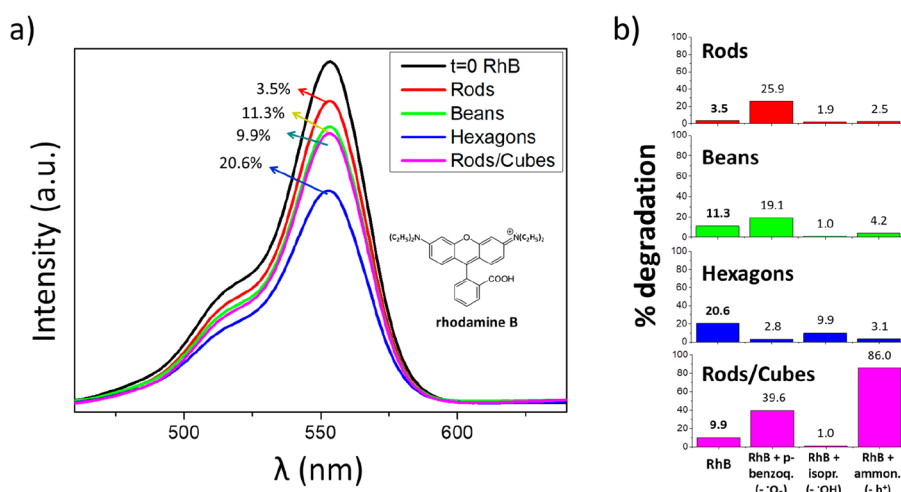


Figure 5. Photocatalytic activity for the degradation of Rh-B dye: (a) absorption spectra for the dye before the start of the photocatalysis, showing the molecule (insert) and photocatalytic activity after 60 min of degradation with different particles of CeO₂; (b) photocatalysis using scavengers for ·O₂ (benzoquinone), ·OH (isopropanol), and h⁺ (ammonium oxalate).

corresponding TA and F_{2g} modes, respectively. The F_{2g} mode in the spectra of the hexagon morphology is predominantly narrow.

Displacements of the Raman bands are associated with phonon confinement, particle size heterogeneity, dopants, crystal lattice stress, and defects.^{41,42} Considering that the samples are undoped CeO₂ and have a homogeneous particle size (Figure 1), the observed shift in the Raman spectra is associated with the defects resulting from the preferred orientation that the particles are grown. In addition, relating the D mode, 590 cm⁻¹, with the F_{2g} mode, the relative concentration of oxygen vacancies can be found by the ratio ($A_D/A_{F_{2g}}$) × 100. Its magnitude follows the order CeO₂ beans (9.9) > CeO₂ rods (9.1) > CeO₂ rods/cubes (8.4) > CeO₂ hexagons (2.4). It is observed that the sample grown in the bean-type morphology, which is an expanded sphere along one of the axes, presents (111) and (200) orientations, implying that there is freedom for the growth of the morphology along the axis, *h*00. This is a consequence of the displacement of the F_{2g} mode to a lower energy resulting in the degree of freedom of the structure and to the larger ratio of the oxygen vacancies. If the band related to the F_{2g} mode has the shift to a higher energy up to the sample spectrum of the hexagon type, then it is pertinent to relate that the shift is related to the structure with the largest number of exposed planes of (111), (220), and (311), among the others. This results in a particle with the highest symmetry, which is observed both in the F_{2g} mode shifting to a higher energy, representing stronger metal–oxygen bond vibration, and in the smaller $A_D/A_{F_{2g}}$ ratio. The smaller number of bands is another indication of the higher symmetry for the hexagonal sample.

The chemical states, defects, and surface compositions of the different morphologies obtained were analyzed by XPS. The survey spectra of different CeO₂ morphologies are shown in Figure S2. Ce and O elements are present in the regions of 890 and 530 eV, respectively. Although all samples have a bulk CeO₂ phase, the surface defects are varied according to the exposed surface, as can be observed in the slight difference in the shape of the peaks for O 1s, Figure 3b. The O 1s spectra of CeO₂ can be deconvoluted into three peaks, located at ~529, ~531, and ~533 eV. The peak at lower binding energy (BE) was ascribed to the Ce–O bond, the middle one is related to

hydroxide and surface defects (–OH, V_o), and the highest was assigned to oxygen-bonded carbon species (C–O, C=O).^{43,44} Values for the position and area percentage of each peak are given within the figure. Overall, the percentage of defect-related peak (BE ~ 531 eV) is similar for all samples. However, in relation to the proportion of lattice-bound oxygen (BE ~ 529 eV), there is a difference between the samples. The proportion is similar for rod and hexagon samples (41%), higher for beans (43%), and the lowest proportion is found for the rod/cube sample (28%). The proportion of oxygen bound to the crystal lattice may be related to the variation between the Ce⁴⁺ and Ce³⁺ proportions on the surface. Therefore, it is expected that the rod/cube sample may have a higher Ce³⁺ ratio, as can also be estimated by the displacement to lower energy of the high resolution peak for this sample (Figure S3).

4.2. Photocatalytic Activity and Identification of Active Species. Photocatalytic tests using the different CeO₂ morphologies described before were performed for degradation of the CIP drug and Rh-B dye solutions, as shown in Figures 4 and 5, respectively. The figures show the spectra measured before starting the photocatalytic test (*t* = 0) and after 60 min of the experiment, and the adsorption and degradation tests performed at different times and rate constant are shown in Figure S4 and Table 1. Figure 4a exhibits the CIP absorption spectrum (*t* = 0 Cipro) and shows bands in the regions of 220 nm, 275 nm, and 315–330 nm corresponding to the transitions of the aromatic ring, $\pi \rightarrow \pi^*$, and non-ligand $\rightarrow \pi^*$, respectively. In the spectrum of CIP degraded by the rod-type and bean-type CeO₂ particles, there is a hyperchromic shift in the region at 315–300 nm compared

Table 1. Summary Report on Surface Area and Photocatalytic Test (Adsorption and Discoloration) Results for Different CeO₂ Morphologies

sample	BET surface area (m ² /g)	Langmuir surface area (m ² /g)	adsorption (%)	photocatalytic activity (%)
rod	228.38	334.08	9.08	3.47
bean	152.25	223.02	2.23	11.27
hexagon	156.59	236.39	4.47	20.63
rod/cube	206.82	307.94	8.65	9.94

to the spectrum before starting the photocatalytic test ($t = 0$). The spectrum for degradation of the drug using the hexagon-type CeO₂ particles shows a hyperchromic shift for all the bands of the spectrum. In the spectrum of CIP degraded by the rod/cubes-type CeO₂ particles, there are no significant changes, only reduction of absorption intensity compared to spectrum before degradation, allowing determination of the Langmuir–Hinshelwood kinetics⁴⁵ with a rate constant of $3.9 \times 10^{-3} \text{ min}^{-1}$ (Figure S4c), according to the values found in the literature for CeO₂ pure.^{10,46} These results demonstrate that the degradation is not complete because commonly in photocatalytic experiments, a gradual reduction in all the absorption bands is observed.⁴⁷ However, the most interesting observation is that when using pure CeO₂ particles and changing only their morphology, different spectra were generated for each type of particle after the photocatalysis. Moreover, since the CIP molecule (inset in Figure 4a) has multiple functional groups, such as secondary alkylamine, two tertiary arylamines (aniline type amines), and a carboxylic acid, it presents an amphoteric behavior: basic part in the secondary alkylamine and acidic part in the carboxylic acid;²² therefore, it is possible to determine which surface is related to each part of the degradation of the molecule.

For this, analysis of the intermediates of the CIP degradation helps to better understand the details of the reaction process. Therefore, mass spectroscopic analyses (Figure 4b, Table S1) were performed for the original solution of the drug and degraded aliquots in the photocatalytic test. Peak m/z 332 corresponds to CIP (M^+), and the other peaks are the intermediates generated during the degradation. For the rod-type morphology, the degradation of CIP occurs in a high incidence generating intermediate ion m/z 279 (M^+) (Figure 4c) by the cleavage of the N- Δ group, corresponding to the breakdown of the $n \rightarrow \pi^*$ bonds. This is consistent with the observed hyperchromic shift in the UV–vis spectrum. The sample degraded by the bean-type morphology indicates an intense ion at m/z 288 (M^+), indicating that there is a high incidence of the breaking of the carboxylic acid group of the CIP molecule, related to the breaking of the $\pi \rightarrow \pi^*$ and non-ligand $\rightarrow \pi^*$ groups. The sample degraded by the hexagonal morphology shows ions at m/z 288 (M^+) and m/z 157 (M^+), the first related to the breakdown of the carboxylic acid group and the second related to the intermediate aromatic groups.⁴⁸ For the degradation using the rod/cube morphology, the mass analysis shows a low intensity for the formation of ion m/z 288 (M^+) corresponding to a CO₂ loss, indicating a low degradation efficiency. The conclusions of the analysis are consistent with the results obtained from the shifts in the UV–vis absorption spectra.

To verify the photocatalytic efficiency of CeO₂ in the degradation of a molecule with a simpler structure compared to the CIP molecule, photocatalytic tests were performed using Rh-B, as shown in Figure 5. This molecule is a common dye in the triphenylmethane family and contains four *N*-ethyl groups on both sides of the xanthen ring⁴⁹ (inset of Figure 5a). The percentage of discoloration after 60 min of the photocatalytic test for each CeO₂ morphology is indicated in Figure 5a and Table 1. It is observed that the photocatalytic efficiency is different for each morphology, rod-CeO₂ < rod/cube-CeO₂ < bean-CeO₂ < hexagon-CeO₂, and presents a logical relation with the rate constant, in which the higher one was found for the hexagon-CeO₂ sample, $6.3 \times 10^{-3} \text{ min}^{-1}$ (Figure S4b). These experiments allow us to determine how each

morphology affects the photocatalytic efficiency of the CeO₂ nanoparticles.

The mechanism of photocatalysis using a semiconductor is attributed to the oxidative stress induced by oxygen reactive species (ORS) such as superoxide radicals, O₂^{-•}, hydroxyl radicals, OH[•], and h⁺. To complete the photocatalytic study, experiments were performed to determine the active species generated during the photocatalyst tests (Figure 5b). The experiments were conducted using scavengers, which act by capturing O₂^{-•}, OH[•], and h⁺, using *p*-benzoquinone, isopropyl alcohol, and ammonium oxalate scavengers, respectively. Rh-B with absorption in the visible region was employed as standard in this test, since CIP has absorption in the scavengers region. It is important to highlight before analyzing the following experiments that when materials with low photocatalytic activity are tested with scavengers, the recombination of the charge carriers is prevented, and the photocatalytic activity is increased.^{15,50} For a complete discussion of the results, we will show the analysis in a graph with a column form, comparing the effect of each scavenger for different morphologies and of each morphology by the use of scavengers.

The first column in Figure 5b shows the photocatalytic activity of the materials without the use of scavengers, and the second, third, and fourth columns show the same using the O₂^{-•}, OH[•], and h⁺ scavengers, respectively. The results illustrate that these semiconductors have a low activity as a function of the morphology. In the second column, using the O₂^{-•} radical scavenger, corresponding to the formation of photogenerated electrons, it is verified that the surfaces most affected by the lack of the superoxide radical is that of the hexagon morphology. Contrastingly, the bean, rod, and rod/cube morphologies become more active with the elimination of the electrons, having an action that is more effective by holes. This suggests that the surface with hexagon morphology has the most tendency to generate electrons. In the third column, using the scavenger for the OH[•] radicals, which are generated by an intermediate reaction of the holes, it is verified that the surfaces most affected by the lack of the hydroxyl radicals are those of the bean and rod/cube morphologies, followed by those of the rod and hexagon morphologies. It is important to note at this point that the hexagon surface has the least participation of hydroxyl radicals in the photocatalytic process. Finally, in the fourth column, using the scavenger for h⁺, it is verified that the surfaces most affected are of the rod, hexagon, and bean morphologies, respectively. The rod/cubes morphology has a stronger action by the elimination of holes. In this case, the electron/hole interaction is stronger.

By analyzing based on the graph for each morphology and comparing with the photocatalytic activity without the use of scavengers, it is found that for rods, with the use of scavengers for the OH[•] radical and h⁺ there is no significant change, implying that these species are barely produced for this morphology. With the use of the scavenger for O₂^{-•} in turn, the photoactivity increases approximately 10 times compared to that without the use of the scavenger, suggesting that this morphology produces a high density of electrons; however, it has a high rate of recombination on the surface.¹⁵ This is in agreement with the analysis based on the columns showing that this morphology becomes more active by the elimination of electrons. In the graph for the sample of the bean morphology, the use of the scavenger for O₂^{-•} radicals causes a photocatalytic activity increase of 70% compared to that without the use of the scavenger. With the use of the OH[•]

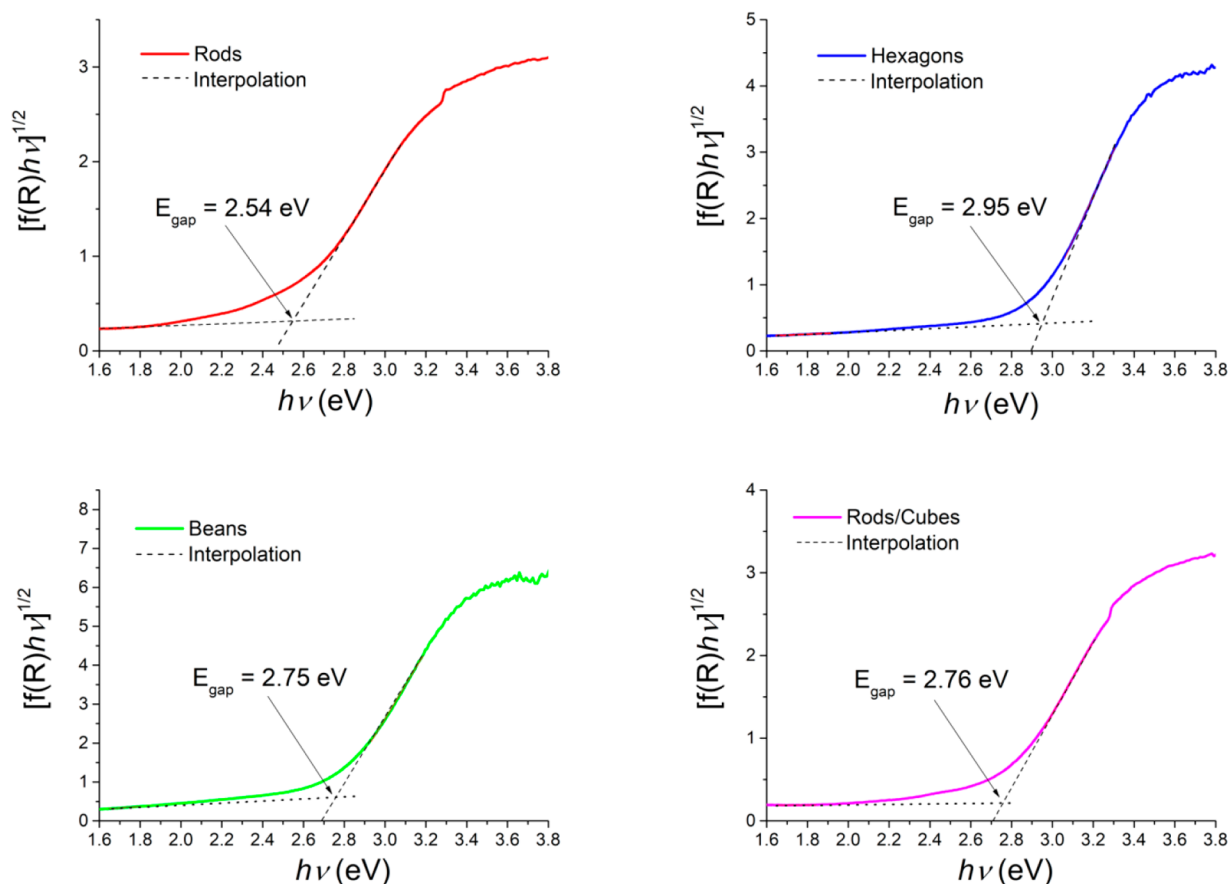


Figure 6. Tauc plot of the CeO₂ samples with rod-, hexagon-, bean-, and rod/cube-type morphologies. Band gap energies are 2.54 eV for the rod-type morphology, 2.75 eV for the bean-type morphology, 2.76 eV for the rod/cube-type morphology, and 2.95 eV for the hexagon-type morphology.

radical scavenger and h⁺ scavenger, there is a reduction in the photocatalytic activity of 91% and 62%, respectively. This indicates that both e⁻ and h⁺ are formed in this morphology, but the e⁻, as also in the previous morphology, has a high rate of recombination. The highest degradation rate obtained for the standard is 21% and found for CeO₂ with the hexagon-type morphology. It is observed from the scavenger analyses that for both the agents O₂^{-•} radical and h⁺, the degradation rate drops by 90%, indicating that the surface produces both electrons and holes and without significant recombination. For CeO₂ with the rod/cube-type morphology, the photodegradation of the pattern is 10%, and the effect of the use of the scavengers for the O₂^{-•} radical and h⁺ is similar to that for the sample of hexagon type; however, there is an increase in the photodegradation rate. This indicates that in this morphology both electrons and holes are produced but with a high recombination rate and a higher production of holes compared to those in all the samples. Therefore, these data reveal the tendency of the morphologies to form charge carriers. These can be ordered as hexagon morphology to form e⁻ = h⁺, rod morphology to form e⁻ > h⁺, bean morphology to form h⁺ > e⁻, and rod/cube morphology to form e⁻ ≅ h⁺.

Therefore, each type of CeO₂ morphology acts differently in the degradation of the drug and dye. In the CIP, with distinct functional groups, the degradation occurs in different groups of the molecule; and to the Rh-B, with similar functional groups, difference in discoloration efficiency occurs. Photocatalytic efficiency should be correlated to the exposed surface type,

since the analyses for specific surface area (Table 1) show that the particles with smaller surface area have the highest photocatalytic activity. From these results it is observed that the adsorption mechanism is directly related to the surface area of the particles, in which higher adsorption is found for the rod and rod/cube particles and a higher photocatalysis for beans and hexagons (Table 1, Figure S4a). It is suggested that photocatalytic activity correlates more with the exposed surface type than with the surface area.^{51,52} The reasons for this difference in the degradation for each morphology are related to the structural defects, as presented previously, and electronic properties, as will be shown below.

4.3. Electronic Structure and Distribution of Surface Charges. Figure 6 shows the Tauc plot obtained from the absorption spectra of the CeO₂ samples with the different morphologies. The Tauc plot determines the band gap energy (E_{gap}) of the all samples from the intercept on the abscissa axis of a linear fit of the $(\alpha h\nu)^{1/2}$ vs wavelength energy plot, where α is the absorbance and $h\nu$ is the photon energy, considering an indirect band gap for CeO₂.⁵³ The E_{gap} values of the samples are shown in the legend in the figure, and the values obtained are smaller than those by the studies that consider the direct band gap,⁵⁴ according to the works that consider an indirect band gap,^{46,53} or calculated by theoretical studies.⁵⁵ Among the samples, CeO₂ with the hexagon-type morphology has the largest E_{gap} . This value is reasoned by the smaller ratio of the oxygen vacancies observed in the Raman analyses, suggesting that there are fewer defects in the structure, and

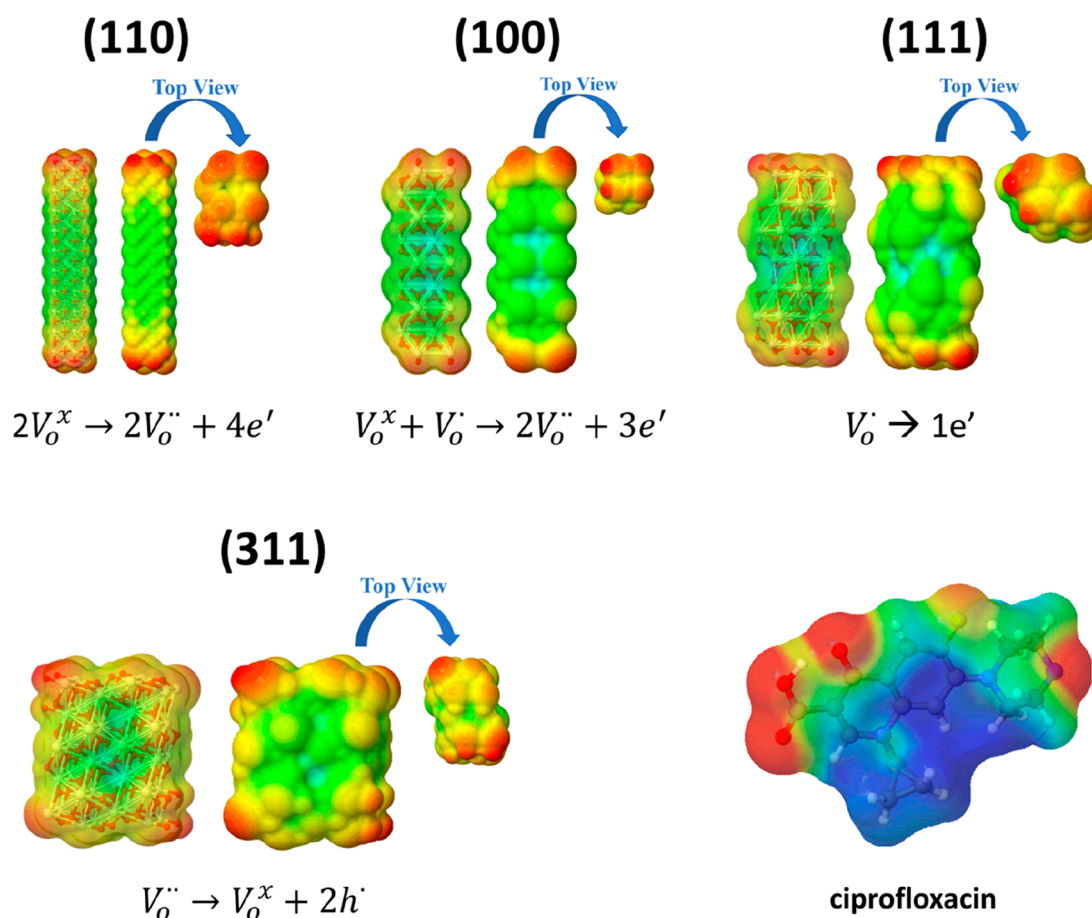


Figure 7. Map of the electrostatic potential obtained by the Mulliken charges of the (100), (110), (111), and (311) surfaces of CeO_2 and ciprofloxacin molecule. The regions of blue and red color represent positive and negative charges of the surfaces.

thus, a larger E_{gap} . Following this reasoning, it is expected that the sample with the bean-type morphology (with a large oxygen vacancy ratio in the Raman analysis) will have a small band gap energy but is not observed. The smallest E_{gap} value is found for the rod sample, which also has a larger oxygen vacancy ratio; however, different crystalline planes are exposed in the rods and beans (Figure 1), which influence the E_{gap} .

The theoretical analyses of the optimized surfaces shows that the (111) surface is the most stable surface (Figure 2); in contrast, the theoretically calculated E_{gap} of the (111) surface is the largest, 2.75 eV, followed by 2.67, 2.42, and 2.40 eV for the (311), (110), and (100) surfaces, respectively. In this view, the experimentally observed most exposed surface is the one that predominates in the E_{gap} of the nanoparticle. Thus, the hexagon morphology has a larger influence of the (111) and (311) surfaces, which have a larger E_{gap} and are the greatest contributors to this morphology. The sample with the rod/cube-type morphology, which predominantly has the (111) surface, should have the largest E_{gap} ; however, the existence of two morphologies increases the predominance of defects and reduces the band gap.⁵⁶ The bean type has a small percentage of the (200) surface, with the (111) surface being dominant; therefore, its E_{gap} approaches⁵⁷ the obtained value for the rod/cube morphology. For the rod morphology, the E_{gap} is the smallest, 2.54 eV, owing to the large contribution of the exposed (220) surface, whose E_{gap} is close to the theoretically obtained value, 2.42 eV.

As stated, different exposed surfaces lead to different behaviors, and the coordination number (CN) has a direct relationship with the surface and photocatalysis. In bulk CeO_2 , the CN is (8,4) corresponding to the Ce and O ions, respectively. CeO_2 surfaces have different CNs according to their termination (Figure 2). On the (110) and (100) surfaces, the metal ions form $[\text{CeO}_6]$ clusters, and the CN is 6,3 and 6,4, respectively. The (111) and (311) surfaces have clusters of the type $[\text{CeO}_7]$, and the CN is 7,3 and 7,4, respectively. On the basis of this, the influence of the surface termination, charge distribution of the most exposed atoms of each surface, and photocatalytic activity was analyzed in terms of the theoretical Mulliken charge of each surface atom. The electronic charge of each layer surface was obtained, and the charge distribution of all the surfaces was analyzed (Table S2). Additionally, the electrostatic potential maps were plotted to evaluate and complement the analysis of the charge distribution, as shown in Figure 7.

As expected, the four surfaces have a well spread charge distribution in the inner layers, with a different charge distribution observed in the first layer. Regions with high electron density are shown as red spots, and regions with a low electron density are displayed as spots from green to blue colors. Although the four surfaces have oxygen in the exposed layer, according to Figure 7, the (311) and (111) surfaces are those in which the first layer is slightly more positive than the other surfaces. Thus, the (311) surface is more positive than the (111) surface. The (100) surface is slightly more negative

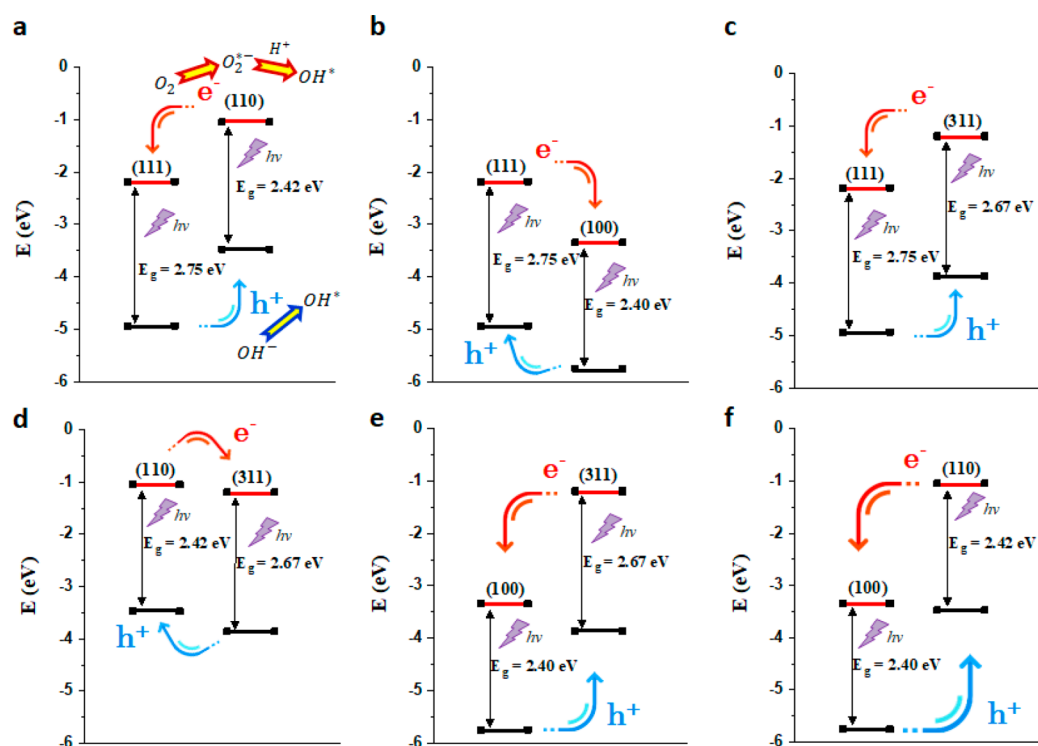


Figure 8. Schematic of the results of the theoretical band alignment and in (a) photogenerated charge transfer process. The left and right parts in each panel represent the level alignment in the possible CeO₂ surfaces: (a) (111)/(110), (b) (111)/(100), (c) (111)/(311), (d) (110)/(311), (e) (100)/(311), (f) (100)/(110). The traces of black color represent the VBM and traces in red the CBM; between these traces, the band gap value for each surface is shown. The arrows represent the possible mobility of the load carriers between the surfaces.

Table 2. Summary of Surface and Photocatalytic Properties of CeO₂ Morphologies

	rod	bean	hexagon	rod/cube
BET specific surface area (m ² ·g ⁻¹)	228.38	152.25	156.59	206.82
exposed planes	(111), (110)	(111), (100)	(111), (110), (311)	(111)
types of [CeO _x] clusters	[CeO ₇] ⁺ ·V _o ^x [CeO ₆] ⁺ ·2V _o ^x	[CeO ₇] ⁺ ·V _o ^x [CeO ₆] ⁺ ·2V _o ^x	[CeO ₇] ⁺ ·V _o ^x [CeO ₆] ⁺ ·2V _o ^x	[CeO ₇] ⁺ ·V _o ^x
electron densities	V _o [*] → 1e' 2V _o ^x → 2V _o ^{**} + 4e'	V _o [*] → 1e' V _o [*] + V _o [*] → 2V _o ^{**} + 3e'	V _o [*] → 1e' 2V _o ^x → 2V _o ^{**} + 4e' V _o ^{**} → V _o [*] + 2h	V _o [*] → 1e'
E _{gap} (eV)	2.54	2.75	2.95	2.76
photochemically generated species	e ⁻ > h ⁺ (with strong interaction)	h ⁺ > e ⁻	e ⁻ = h ⁺	e ⁻ ≅ h ⁺ (with strong interaction)
% discoloration Rh-B	3.5	11.3	20.6	9.9
preferential cleavage on CIP	N-Δ group	carboxylic acid group	aromatic groups	carboxylic acid group (low efficiency)

than the (111) surface, and finally, the (110) surface presents the most negative exposed layer; i.e., the order of the most negative to the positive surface is 110 > 100 > 111 > 311. The highest and lowest electron densities of the (110) and (311) surfaces, respectively, imply that the first surface is an electron donor and the second is a donor of holes. This fact suggests that the surface of the semiconductor can be p (high electronic density) or n (donor of holes) type, although it is an n-type semiconductor. In the present case, the (311) surface behaves as n type, whereas the (110) surface acts as p type. Regarding reactivity, the tendency of a surface to be more positive or more negative reveals whether it will act as a receptor, i.e., an oxidizing agent, or an electron donor, i.e., a reducing agent, respectively, and affect the surface reactivity.⁵⁸

For the CIP molecule, which has multiple functional groups, the electrostatic potential maps (Figure 7) show that the electron density is around the oxygen atoms of COOH, carboxyl terminations, and nitrogen atoms, whereas the

positive density is around the aromatic rings and cyclopropyl group. It is observed in studies related to adsorptive capacity⁵⁹ that regions with a positive (negative) potential of the particle can attract the negative (positive) regions of a molecule. Thus, the positive side of the CIP molecules can have more affinity to the (100) and (110) surfaces, whereas the negative side has more affinity to the (311) and (111) surfaces.

To complete the analyses, the valence band maximum (VBM) and conduction band minimum (CBM) were aligned for each surface by theoretical calculations (see Figure 8) by comparing with the experimental results and considering the photocatalytic processes in which the charge carriers are generated by the excitation of light energy. For instance, the electronic structure at the interface between the (111) and (110) surfaces, depending on how the surface defects are, may result in a process for electron and hole transfer and an efficient charge separation.⁶⁰ The (110) surface with an excited electron in the CBM at -1.04 eV can result in the decay of the

electron to the energy level of -2.18 eV of the CBM of the (111) surface. The formed holes in turn can be transferred from the VBM of the (111) surface, -4.93 eV, to the VBM of the (110) surface, -3.47 eV.^{61–63} Other processes may occur depending on the energy between the bands, such as the recombination of the electrons located in the CBM of a surface with the holes located in the VBM of the adjacent surface⁶⁴ or that can be separated on the surfaces to react with the donor (D) or acceptor (A) species adsorbed on or close to the surfaces, such as H_2O and O_2 . In this case, the h^+ can react with the adsorbed OH^- to produce OH^\bullet radicals. In comparison, an $\text{O}_2^{\bullet-}$ radical is formed when the adsorbed oxygen (O_2) comes into contact with an e^- (Figure 8a).^{65,66}

According to experiments and theoretical models, the photodegradation process varies with each morphology. Photocatalytic activity is dominated by e^- for rod and by h^+ for bean morphology, by h^+/e^- for hexagon, and by OH^\bullet for rod/cube since they have strong h^+/e^- interaction. This is a consequence of the predominant face defect types in the different morphologies ($[\text{CeO}_7\text{-V}_x^\bullet]$, $[\text{CeO}_6\text{-}2\text{V}_x^\bullet]$) and the electron density on each surface which has influence to the recombination of charge carriers, Table 2.

On the basis of the summary of results shown in the Table 2 for the material with the rod morphology, the presence of the high electron density surface allows preferential attack of the positive side of the CIP molecule. However, it results in the lower band gap value which does not prevent the high recombination of the charge carriers, causing a low photocatalytic efficiency for Rh-B. Bean morphology with hole-commanded photocatalytic mechanism improves Rh-B photocatalysis compared to rods, which is plausible since species such as OH^\bullet radicals and photogenerated holes act directly to attack the central carbon of Rh-B causing discoloration of the dye.⁴⁹ To break the CIP molecule, the bean morphology, which presents relative electron density on the surface, cleaves the drug molecule at the carboxylic acid group. This is an organic high electron density group, so the attack preference may be related to (i) the cleavage between the negative (carboxylic acid) and positive (aryl amine) region of CIP²² and (ii) the main species generated (h^+) in the semiconductor interacting with the negative side of the molecule. Hexagon morphology has defects that result in highest and lowest electron density surfaces. It is the sample with the highest band gap energy and the lowest e^-/h^+ recombination rate. These are factors that provide a higher rate of Rh-B degradation and the cleavage in different CIP groups. Rod/cube morphology presents a high proportion of charge carrier recombination; however, the intermediate mechanism of hydroxyl radical generation results in the relative efficiency for Rh-B discoloration and attack on the CIP carboxylic acid group.

Therefore, it can be inferred that the more oxidant or reducing surfaces cause retardation of the e^-/h^+ recombination, whereas the intermediate surfaces between positive/negative types have a high rate of e^-/h^+ recombination. According to the literature, the reason the diverse facets behave as oxidation and reduction sites is that surface energy levels of the CBs and VBs of the facets are dissimilar, i.e., the E_{gap} is different. Therefore, the photoexcited e^- and h^+ can be driven to different facets, leading to their separation. Some works typically associate a superior photocatalytic activity to a low percentage of undercoordinated atoms on the crystal surface. However, this work shows that the photocatalytic behavior is not only owing to the percentage of under-

coordinated or coordinated atoms on the surface but also because of the cooperative mechanism combining favorable surface atomic structures (coordination atoms) and surface electronic structures (band gap).

5. CONCLUSIONS

In this paper, we presented a study on the relationship between the rod, bean, hexagon, and rod/cube morphologies of CeO_2 with the exposure of the (111), (110), (100), and (311) surfaces and the main charge carriers generated by the photochemical process. By using scavengers, it was found that the reactive species were changed with different morphologies. Theoretical studies based on the DFT showed that the charge distribution, band gap, types of defects, and band alignment were specific for each surface. Particles with simultaneous surface exposure with higher and lower electron density were found to decrease the recombination of charge carriers. The highest degradation rate was achieved by hexagon-shaped CeO_2 samples. These particles present the surfaces with the highest (110) and lowest (311) electron density, in addition to the surface (111). Scavenger analyses showed that when capture agents of $\text{O}_2^{\bullet-}$ radical and h^+ are used, the photocatalytic activity decreases; i.e., electrons and holes are simultaneously produced on the surface without recombination.

Therefore, the differences between the electron density, band gap energy, and the band alignment of the exposed surfaces in particles are responsible for the greatest separation of charge carriers in an undoped and unmodified semiconductor. The relationship between morphology with exposed surface and surface defects results in photochemically generated species, which is correlated with the preferential attack on the CIP molecule. More negative surfaces act as a reducing agent and result in the degradation of more positive regions of the molecule to be degraded. This indicates that a morphological control to the exposed surfaces of CeO_2 with different atomic structures allows the development of a more efficient and innovative strategy to tune the photocatalyst selectivity. In addition, the results show that tuning the crystal facets allows for optimal photocatalytic reactivity and achieving a selectivity degradation pathway. Tests by photocatalytic cycles should be performed in order to verify the reusability of the semiconductor. We believe these results will help the development and optimization of pure semiconductors and, from these, the proposition of doping or composite research to further improve properties.

■ ASSOCIATED CONTENT

Supporting Information

The Supporting Information is available free of charge on the ACS Publications website at DOI: 10.1021/acsanm.9b01452.

Long-range X-ray diffraction analyses of the nanoparticles obtained by the microwave-assisted hydrothermal synthesis, XPS survey and Ce 3d spectra, description of Langmuir–Hinshelwood model, adsorption/degradation tests performed at different times and rate constant, monoisotopic mass (Da) and structures related to possible intermediates CIP, and Mulliken charges obtained for the atoms of the first monolayer of the surfaces (PDF)

AUTHOR INFORMATION

Corresponding Author

*E-mail: rafaeldciola@yahoo.com.br; rciola@uji.es. Phone: +55 12 3123 2228.

ORCID

Rafael A. C. Amoresi: 0000-0002-7523-6013

Regiane C. Oliveira: 0000-0002-7332-8731

Elson Longo: 0000-0001-8062-7791

Julio R. Sambrano: 0000-0002-5217-7145

Notes

The authors declare no competing financial interest.

ACKNOWLEDGMENTS

The authors E.L., M.A.Z., J.R.S., and A.Z.S. thank the CEPID/CDMF, São Paulo Research Foundation, FAPESP Proc., Grant 2013/07296-2. The author N.L.M. thanks the FAPESP Proc., Grants 2016/07476-9 and 2016/25500-4, and the author R.A.C.A. thanks the FAPESP Proc., Grants 2017/19143-7 and 2019/09296-6. All the authors thank the National Council for Scientific and Technological Development (CNPq) for the financial support granted in the course of this research. We are also grateful to the LMA-IQ for providing the FEG-SEM facilities.

REFERENCES

- (1) Li, Q.; Li, X.; Li, W.; Zhong, L.; Zhang, C.; Fang, Q.; Chen, G. Effect of Preferential Exposure of Anatase TiO₂ {001} Facets on the Performance of Mn-Ce/TiO₂ Catalysts for Low-temperature Selective Catalytic Reduction of NO_x with NH₃. *Chem. Eng. J.* **2019**, *369*, 26–34.
- (2) Wan, J.; Lin, J.; Guo, X.; Wang, T.; Zhou, R. Morphology Effect on the Structure-Activity Relationship of Rh/CeO₂/ZrO₂ Catalysts. *Chem. Eng. J.* **2019**, *368*, 719–729.
- (3) de Oliveira, R. C.; de Foggi, C. C.; Teixeira, M. M.; da Silva, M. D. P.; Assis, M.; Francisco, E. M.; da Silva Pimentel, B. N. A.; dos Santos Pereira, P. F.; Vergani, C. E.; Machado, A. L.; Andres, J.; Gracia, L.; Longo, E. Mechanism of Antibacterial Activity via Morphology Change of α -AgVO₃: Theoretical and Experimental Insights. *ACS Appl. Mater. Interfaces* **2017**, *9*, 11472–11481.
- (4) Li, D.; Chen, S.; You, R.; Liu, Y.; Yang, M.; Cao, T.; Qian, K.; Zhang, Z.; Tian, J.; Huang, W. Titania-Morphology-Dependent Dual-Perimeter-Sites Catalysis by Au/TiO₂ Catalysts in Low-Temperature CO Oxidation. *J. Catal.* **2018**, *368*, 163–171.
- (5) Ribeiro, R. A. P.; Lacerda, L. H. S.; Longo, E.; Andrés, J.; De Lazaro, S. R. Towards Enhancing the Magnetic Properties by Morphology Control of ATiO₃ (A = Mn, Fe, Ni) Multiferroic Materials. *J. Magn. Magn. Mater.* **2019**, *475*, 544–549.
- (6) Pereira, P. F. S.; Gouveia, A. F.; Assis, M.; de Oliveira, R. C.; Pinatti, I. M.; Penha, M.; Gonçalves, R. F.; Gracia, L.; Andres, J.; Longo, E. ZnWO₄ Nanocrystals: Synthesis, Morphology, and Photoluminescence and Photocatalytic Properties. *Phys. Chem. Chem. Phys.* **2018**, *20*, 1923–1937.
- (7) Mai, H.-X.; Sun, L.-D.; Zhang, Y.-W.; Si, R.; Feng, W.; Zhang, H.-P.; Liu, H.-C.; Yan, C.-H. Shape-Selective Synthesis and Oxygen Storage Behavior of Ceria Nanopolyhedra, Nanorods, and Nanocubes. *J. Phys. Chem. B* **2005**, *109*, 24380–24385.
- (8) Warule, R. M. S. S.; Chaudhari, N. S.; Kale, B. B.; Patil, K. R.; Koinkar, P. M.; More, M. A.; Murakami, R.-i. Organization of Cubic CeO₂ Nanoparticles on the Edges of Self Assembled Tapered ZnO Nanorods via a Template Free One-Pot Synthesis: Significant Cathodoluminescence and Field Emission Properties. *J. Mater. Chem.* **2012**, *22*, 8887–8895.
- (9) Liu, J.; Dai, M.; Wang, T.; Sun, P.; Liang, X.; Lu, G.; Shimano, K.; Yamazoe, N. Enhanced Gas Sensing Properties of SnO₂ Hollow Spheres Decorated with CeO₂ Nanoparticles Heterostructure

Composite Materials. *ACS Appl. Mater. Interfaces* **2016**, *8*, 6669–6677.

(10) Ma, R.; Zhang, S.; Li, L.; Gu, P.; Wen, T.; Khan, A.; Li, S.; Li, B.; Wang, S.; Wang, X. Enhanced Visible-Light-Induced Photoactivity of Type-II CeO₂/g-C₃N₄ Nanosheet Toward Organic Pollutants Degradation. *ACS Sustainable Chem. Eng.* **2019**, *7*, 9699–9708.

(11) Feng, Z.; Ren, Q.; Peng, R.; Mo, S.; Zhang, M.; Fu, M.; Chen, L.; Ye, D. Effect of CeO₂ Morphologies on Toluene Catalytic Combustion. *Catal. Today* **2019**, *332*, 177–182.

(12) Ma, R.; Zhang, S.; Wen, T.; Gu, P.; Li, L.; Zhao, G.; Niu, F.; Huang, Q.; Tang, Z.; Wang, X. A Critical Review on Visible-Light-Response CeO₂-based Photocatalysts with Enhanced Photooxidation of Organic Pollutants. *Catal. Today* **2019**, *335*, 20–30.

(13) Lv, Y.; Huang, K.; Zhang, W.; Yang, B.; Chi, F.; Ran, S.; Liu, X. One Step Synthesis of Ag/Ag₃PO₄/BiPO₄ Double-Heterostructured Nanocomposites with Enhanced Visible-Light Photocatalytic Activity and Stability. *Ceram. Int.* **2014**, *40*, 8087–8092.

(14) Zhang, W.; Hu, C.; Tan, J.; Fan, Z.; Chi, F.; Sun, Y.; Ran, S.; Liu, X.; Lv, Y. Novel α -FeOOH Nanorods/Ag₃PO₄ Semiconductor Composites with Enhanced Photocatalytic Activity and Stability. *Nano* **2016**, *11*, 1650071.

(15) Coletto, U., Jr; Amoresi, R. A. C.; Teodoro, V.; Iani, I. M.; Longo, E.; Zaghete, M. A.; Perazolli, L. A. An Approach for Photodegradation Mechanism at TiO₂/SrTiO₃ Interface. *J. Mater. Sci.: Mater. Electron.* **2018**, *29*, 20329–20338.

(16) Fujishima, A.; Zhang, X.; Tryk, D. A. TiO₂ Photocatalysis and Related Surface Phenomena. *Surf. Sci. Rep.* **2008**, *63*, 515–582.

(17) Hashimoto, K.; Irie, H.; Fujishima, A. TiO₂ Photocatalysis: A Historical Overview and Future Prospects. *Jpn. J. Appl. Phys.* **2005**, *44*, 8269–8285.

(18) Li, Y. Y.; Zhou, B. X.; Zhang, H. W.; Ma, S. F.; Huang, W. Q.; Peng, W.; Hu, W.; Huang, G. F. Doping-Induced Enhancement of Crystallinity in Polymeric Carbon Nitride Nanosheets to Improve their Visible-Light Photocatalytic Activity. *Nanoscale* **2019**, *11*, 6876–6885.

(19) Serrà, A.; Zhang, Y.; Sepúlveda, B.; Gómez, E.; Nogués, J.; Michler, J.; Philippe, L. Highly Active ZnO-based Biomimetic Fern-like Microleaves for Photocatalytic Water Decontamination Using Sunlight. *Appl. Catal., B* **2019**, *248*, 129–146.

(20) Saleh, R.; Taufik, A.; Prakoso, S. P. Fabrication of Ag₂O/TiO₂ Composites on Nanographene Platelets for the Removal of Organic Pollutants: Influence of Oxidants and Inorganic Anions. *Appl. Surf. Sci.* **2019**, *480*, 697–708.

(21) Wu, T.; Liu, G.; Zhao, J.; Hidaka, H.; Serpone, N. Photoassisted Degradation of Dye Pollutants. V. Self-Photosensitized Oxidative Transformation of Rhodamine B under Visible Light Irradiation in Aqueous TiO₂ Dispersions. *J. Phys. Chem. B* **1998**, *102*, 5845–5851.

(22) Zavod, R. M.; Knittel, J. J. Drug Design and Relationship of Functional Groups to Pharmacologic Activity. In *Foye's Principles of Medicinal Chemistry*; Lippincott Williams & Wilkins: Philadelphia, 2012; Chapter 2, pp 29–37.

(23) Liu, Z.; Sun, P.; Pavlostathis, S. G.; Zhou, X.; Zhang, Y. Bioresource Technology Adsorption, Inhibition, and Biotransformation of Ciprofloxacin under Aerobic Conditions. *Bioresour. Technol.* **2013**, *144*, 644–651.

(24) Wen, X.; Niu, C.; Zhang, L.; Liang, C.; Guo, H.; Zeng, G. Photocatalytic Degradation of Ciprofloxacin by a Novel Z-Scheme CeO₂-Ag/AgBr Photocatalyst: Influencing Factors, Possible Degradation Pathways, and Mechanism Insight. *J. Catal.* **2018**, *358*, 141–154.

(25) Fei, Y.; Li, Y.; Han, S.; Ma, J. Adsorptive Removal of Ciprofloxacin by Sodium Alginate/Graphene Oxide Composite Beads from Aqueous Solution. *J. Colloid Interface Sci.* **2016**, *484*, 196–204.

(26) Rakshit, S.; Sarkar, D.; Elzinga, E. J.; Punamiya, P.; Datta, R. Mechanisms of Ciprofloxacin Removal by Nano-Sized Magnetite. *J. Hazard. Mater.* **2013**, *246–247*, 221–226.

- (27) Manaia, C. M.; Novo, A.; Coelho, B.; Nunes, O. C. Ciprofloxacin Resistance in Domestic Wastewater Treatment Plants. *Water, Air, Soil Pollut.* **2010**, *208*, 335–343.
- (28) Jiang, J.; Zhou, Z.; Pahl, O. Preliminary Study of Ciprofloxacin (CIP) Removal by Potassium Ferrate (VI). *Sep. Purif. Technol.* **2012**, *88*, 95–98.
- (29) Song, S.; Xu, L.; He, Z.; Chen, J.; Xiao, X.; Yan, B. Mechanism of the Photocatalytic Degradation of C. I. Reactive Black 5 at pH 12.0 Using SrTiO₃/CeO₂ as the Catalyst. *Environ. Sci. Technol.* **2007**, *41*, 5846–5853.
- (30) Chen, F.; Cao, Y.; Jia, D. Preparation and Photocatalytic Property of CeO₂ Lamellar. *Appl. Surf. Sci.* **2011**, *257*, 9226–9231.
- (31) Erba, A.; Baima, J.; Bush, I.; Orlando, R.; Dovesi, R. Large-Scale Condensed Matter DFT Simulations: Performance and Capabilities of the CRYSTAL Code. *J. Chem. Theory Comput.* **2017**, *13*, 5019–5027.
- (32) Demichelis, R.; Civalleri, B.; Ferrabone, M.; Dovesi, R. On the Performance of Eleven DFT Functionals in the Description of the Vibrational Properties of Aluminosilicates. *Int. J. Quantum Chem.* **2010**, *110*, 406–415.
- (33) Corno, M.; Busco, C.; Civalleri, B.; Ugliengo, P. Periodic ab Initio Study of Structural and Vibrational Features of Hexagonal Hydroxyapatite Ca₁₀(PO₄)₆(OH)₂. *Phys. Chem. Chem. Phys.* **2006**, *8*, 2464–2472.
- (34) Graciani, J.; Márquez, A. M.; Plata, J. J.; Ortega, Y.; Hernández, N. C.; Meyer, A.; Zicovich-Wilson, C. M.; Sanz, J. F. Comparative Study on the Performance of Hybrid DFT Functionals in Highly Correlated Oxides: The Case of. *J. Chem. Theory Comput.* **2011**, *7*, 56–65.
- (35) Chen, S.; Cao, T.; Gao, Y.; Li, D.; Xiong, F.; Huang, W. Probing Surface Structures of CeO₂, TiO₂, and Cu₂O Nanocrystals with CO and CO₂ Chemisorption. *J. Phys. Chem. C* **2016**, *120*, 21472–21485.
- (36) Wulff, G. Zur Frage der Geschwindigkeit des Wachstums und der Auflösung der Kristallflächen (On the Question of Speed of Growth and Dissolution of Crystal Surfaces). *Z. Kristallogr. - Cryst. Mater.* **1901**, *34*, 449–530.
- (37) Cölfen, H.; Mann, S. Higher-Order Organization by Mesoscale Self-Assembly and Transformation of Hybrid Nanostructures. *Angew. Chem., Int. Ed.* **2003**, *42*, 2350–2365.
- (38) Hsu, P. W.; RÖnnquist, L.; Matijević, E. Preparation and Properties of Monodispersed Colloidal Particles of Lanthanide Compounds. 2. Cerium(IV). *Langmuir* **1988**, *4*, 31–37.
- (39) Weber, W. H.; Hass, K. C.; McBride, J. R. Raman Study of CeO₂: Second-Order Scattering, Lattice Dynamics, and Particle-Size Effects. *Phys. Rev. B: Condens. Matter Mater. Phys.* **1993**, *48*, 178.
- (40) Schilling, C.; Hofmann, A.; Hess, C.; Ganduglia-Pirovano, M. V. Raman Spectra of Polycrystalline CeO₂: A Density Functional Theory Study. *J. Phys. Chem. C* **2017**, *121*, 20834–20849.
- (41) Golubovic, A.; Scepanovic, M.; Kremenovic, A.; Askrabic, S.; Berec, V.; Dohcevic-Mitrovic, Z.; Popovic, Z. V. Raman Study of the Variation in Anatase Structure of TiO₂ Nanopowders Due to the Changes of Sol-Gel Synthesis Conditions. *J. Sol-Gel Sci. Technol.* **2009**, *49*, 311–319.
- (42) Campbell, I. H.; Fauchet, P. M. The Effects of Microcrystal Size and Shape on the One Phonon Raman Spectra of Crystalline Semiconductors. *Solid State Commun.* **1986**, *58*, 739–741.
- (43) Huang, Y.; Long, B.; Tang, M.; Rui, Z.; Balogun, M.; Tong, Y.; Ji, H. Bifunctional Catalytic Material: An Ultrastable and High-Performance Surface Defect CeO₂ Nanosheets for Formaldehyde Thermal Oxidation and Photocatalytic Oxidation. *Appl. Catal., B* **2016**, *181*, 779–787.
- (44) Chen, F.; Ho, P.; Ran, R.; Chen, W.; Si, Z.; Wu, X.; Weng, D.; Huang, Z.; Lee, C. Synergistic Effect of CeO₂ modified TiO₂ Photocatalyst on the Enhancement of Visible Light Photocatalytic Performance. *J. Alloys Compd.* **2017**, *714*, 560–566.
- (45) Costa, C. N.; Christou, S. Y.; Georgiou, G.; Efstathiou, A. M. Mathematical Modeling of the Oxygen Storage Capacity Phenomenon Studied by CO Pulse Transient Experiments Over Pd/CeO₂ Catalyst. *J. Catal.* **2003**, *219*, 259–272.
- (46) Channei, D.; Inceesungvorn, B.; Wetchakun, N.; Ukritnukun, S.; Nattestad, A.; Chen, J.; Phanichphant, S. Photocatalytic Degradation of Methyl Orange by CeO₂ and Fe-doped CeO₂ Films under Visible Light Irradiation. *Sci. Rep.* **2015**, *4*, 5757.
- (47) Kumar, J. V.; Karthik, R.; Chen, S.; Muthuraj, V.; Karuppiah, C. Fabrication of Potato-like Silver Molybdate Microstructures for Photocatalytic Degradation of Chronic Toxicity Ciprofloxacin and Highly Selective Electrochemical Detection of H₂O₂. *Sci. Rep.* **2016**, *6*, 34149.
- (48) Liu, T.; Wang, L.; Lu, X.; Fan, J.; Cai, X.; Gao, B.; Miao, R.; Wang, J.; Lv, Y. Comparative Study of the Photocatalytic Performance for the Degradation of Different Dyes by ZnLn₂S₄: Adsorption, Active Species, and Pathways. *RSC Adv.* **2017**, *7*, 12292–12300.
- (49) Yu, K.; Yang, S.; He, H.; Sun, C.; Gu, C.; Ju, Y. Visible Light-Driven Photocatalytic Degradation of Rhodamine B over NaBiO₃: Pathways and Mechanism. *J. Phys. Chem. A* **2009**, *113*, 10024–10032.
- (50) Xian, T.; Yang, H.; Dai, J. F.; Wei, Z. Q.; Ma, J. Y.; Feng, W. J. Photocatalytic Properties of SrTiO₃ Nanoparticles Prepared by a Polyacrylamide Gel Route. *Mater. Lett.* **2011**, *65*, 3254–3257.
- (51) De Oliveira, R. C.; De Foggi, C. C.; Teixeira, M. M.; Da Silva, M. D.; Assis, M.; Francisco, E. M.; Da Silva Pimentel, B. N. A.; Dos Santos Pereira, P. F.; Vergani, C. E.; Machado, A. L.; Andres, J.; Gracia, L.; Longo, E. Mechanism of Antibacterial Activity via Morphology Change of alpha-AgVO₃: Theoretical and Experimental Insights. *ACS Appl. Mater. Interfaces* **2017**, *9*, 11472–11481.
- (52) Macedo, N. G.; Gouveia, A. F.; Roca, R. A.; Assis, M.; Gracia, L.; Andres, J.; Leite, E. R.; Longo, E. Surfactant-Mediated Morphology and Photocatalytic Activity of α -Ag₂WO₄ Material. *J. Phys. Chem. C* **2018**, *122*, 8667–8679.
- (53) Zhou, G.; Yao, Y.; Zhao, X.; Liu, X.; Sun, B.; Zhou, A. Band Gap Energies for White Nanosheets/Yellow Nanoislands/Purple Nanorods of CeO₂. *RSC Adv.* **2016**, *6*, 59370–59374.
- (54) Ortega, P. P.; Rocha, L. S. R.; Cortés, J. A.; Ramirez, M. A.; Buono, C.; Ponce, M. A.; Simões, A. Z. Towards Carbon Monoxide Sensors Based on Europium Doped Cerium Dioxide. *Appl. Surf. Sci.* **2019**, *464*, 692–699.
- (55) Hay, P. J.; Martin, R. L.; Uddin, J.; Scuseria, G. E. Theoretical Study of CeO₂ and Ce₂O₃ using a Screened Hybrid Density Functional. *J. Chem. Phys.* **2006**, *125*, 034712.
- (56) Pereira, W. S.; Ferrer, M. M.; Botelho, G.; Gracia, L.; Nogueira, I. C.; Pinatti, I. M.; Rosa, I. L. V.; La Porta, F. A.; Andres, J.; Longo, E. Effects of Chemical Substitution on the Structural and Optical Properties of α -Ag_{2-2x}Ni_xWO₄ (0 ≤ x ≤ 0.08) solid solutions. *Phys. Chem. Chem. Phys.* **2016**, *18*, 21966–21975.
- (57) Kwong, W. L.; Koshy, P.; Hart, J. N.; Xu, W.; Sorrell, C. C. Critical Role of {002} Preferred Orientation on Electronic Band Structure of Electrodeposited Monoclinic WO₃ Thin Films. *Sustain. Energy Fuels* **2018**, *2*, 2224–2236.
- (58) Wang, L.; Shi, Y.; Yao, D.; Pan, H.; Hou, H.; Chen, J. C.; Crittenden, J. C. Crittenden, Cd Complexation with Mercapto-Functionalized Attapulgite (MATP): Adsorption and DFT Study. *Chem. Eng. J.* **2019**, *366*, 569–576.
- (59) Zhang, F.; Liu, X.; He, X.; Zhao, J.; Chu, W.; Xue, Y. A Periodic Density Functional Theory Study of Adsorption of CO₂ on Anorthite (001) Surface and Effect of Water. *J. Theor. Comput. Chem.* **2019**, *18*, 1950010.
- (60) Li, B.; Si, Y.; Zhou, B.; Fang, Q.; Li, Y.; Huang, W.; Hu, W.; Pan, A.; Fan, X.; Huang, G. Doping-Induced Hydrogen-Bond Engineering in Polymeric Carbon Nitride To Significantly Boost the Photocatalytic H₂ Evolution Performance. *ACS Appl. Mater. Interfaces* **2019**, *11*, 17341–17349.
- (61) André, R. S.; Zamperini, C. A.; Mima, E. G.; Longo, V. M.; Albuquerque, A. R.; Sambrano, J. R.; Machado, A. L.; Vergani, C. E.; Hernandez, A. C.; Varela, J. A.; Longo, E. Antimicrobial Activity of TiO₂:Ag Nanocrystalline Heterostructures: Experimental and Theoretical Insights. *Chem. Phys.* **2015**, *459*, 87–95.
- (62) Hinuma, Y.; Gruneis, A.; Kresse, G.; Oba, F. Band Alignment of Semiconductors from Density-Functional Theory and Many-Body

Perturbation Theory. *Phys. Rev. B: Condens. Matter Mater. Phys.* **2014**, *90*, 155405.

(63) Morkel, M.; Weinhardt, L.; Lohmuller, B.; Heske, C.; Umbach, E.; Riedl, W.; Zweigart, S.; Karg, F. Flat Conduction-Band Alignment at the CdS/CuInSe₂ Thin-Film Solar-Cell Heterojunction. *Appl. Phys. Lett.* **2001**, *79*, 4482.

(64) Marana, N. L.; Casassa, S.; Longo, E.; Sambrano, J. R. Computational Simulations of ZnO@GaN and GaN@ZnO Core@Shell Nanotubes. *J. Solid State Chem.* **2018**, *266*, 217–225.

(65) Liu, C.; Dong, S.; Chen, Y. Enhancement of Visible-Light-Driven Photocatalytic Activity of Carbon Plane/g-C₃N₄/TiO₂ Nanocomposite by Improving Heterojunction Contact. *Chem. Eng. J.* **2019**, *371*, 706–718.

(66) Latha, P.; Prakash, K.; Karuthapandian, S. Enhanced Visible Light Photocatalytic Activity of CeO₂/Alumina Nanocomposite: Synthesized via Facile Mixing-Calcination Method for Dye Degradation. *Adv. Powder Technol.* **2017**, *28*, 2903–2913.